Time-resolved X-ray study of assisted fluidization of cohesive micron powder
On the role of mechanical vibration

Wu, Kaiqiao; Wagner, Evert C.; Ochkin-Koenig, Olga; Franck, Miika; Weis, Dominik; Meesters, Gabrie M.H.; van Ommen, J. Ruud

DOI
10.1016/j.cej.2023.143936

Publication date
2023

Document Version
Final published version

Published in
Chemical Engineering Journal

Citation (APA)
Wu, K., Wagner, E. C., Ochkin-Koenig, O., Franck, M., Weis, D., Meesters, G. M. H., & van Ommen, J. R. (2023). Time-resolved X-ray study of assisted fluidization of cohesive micron powder: On the role of mechanical vibration. *Chemical Engineering Journal*, *470*, Article 143936. https://doi.org/10.1016/j.cej.2023.143936

Chemical Engineering Journal 470 (2023) 143936

Contents lists available at ScienceDirect

Chemical Engineering Journal

journal homepage: www.elsevier.com/locate/cej

Time-resolved X-ray study of assisted fluidization of cohesive micron powder: On the role of mechanical vibration

Kaiqiao Wu [a,*], Evert C. Wagner [a], Olga Ochkin-Koenig [b], Miika Franck [b], Dominik Weis [b], Gabrie M.H. Meesters [a], J. Ruud van Ommen [a,*]

[a] Department of Chemical Engineering, Delft University of Technology, Van der Maasweg 9, Delft 2629HZ, the Netherlands
[b] BASF SE, Carl-Bosch-Straße 38, Ludwigshafen am Rhein 67063, Germany

ARTICLE INFO

Keywords:
Scale-up
Assistance
Gas channel
Vibration
Stratification

ABSTRACT

Mechanical vibration has been broadly used to assist fluidization of cohesive powders, because of its capability to disrupt gas channels and agglomerates. However, the improvement reported in literature is mostly deduced from bulk response and ex-situ measurements, whereas the induced fluidization behavior and underlying physics remain largely unexplored. In this work, the fluidization behavior of micron-sized cohesive silica (Sauter mean diameter D_{32} = 7.9 μm) has been investigated experimentally under vibration of varying conditions. X-ray imaging was carried out to directly capture the temporal evolution of system hydrodynamics, and identify in-situ powder stratification, bubbling and channel formation. The study demonstrates that vibration effectively collapses gas channels, yet facilitates powder stratification and compaction, therefore developing three distinctive flow regions inside the bed with different fluidization states. Consequently, common measurements, such as pressure drop and bed expansion, tend to overestimate the improvement. In addition, increasing frequency, from 10 Hz to 30 Hz, is observed to increase the number of bubbles by 60 %, whereas a large amplitude (e.g., 2 mm) leads to a 10 % compaction in the top flow region.

1. Introduction

Fluidization is one of the most broadly used solid processing techniques in the industry, as it excels in creating homogeneous mixing of solids and offers superior interphase heat and mass transfer. Fine powders, with an extremely high specific surface area, are of great interest for a wide range of applications in pharmaceutical, catalytic and functional material production, but their fluidization is problematic due to the cohesive nature [1–3]. Inter-particle forces, such as capillary force and van der Waals force, become significant at this particle scale. In a typical fluidized bed, fine powders adhere and tend to constitute internal cracks and channels, which bypass a significant portion of the fluidizing gas, resulting in poor interaction between the gas and solid phase. Additionally, the pronounced inter-particle forces also promote agglomeration [4], and discourage overall mixing of solids and bulk circulation. As a result, fine cohesive powders remain largely stagnant even if supplied with a sufficiently large steady gas flow.

Introducing additional degrees of freedom offers flexibility to manipulate fluidization. Over the last decades, researchers proposed several so-called “assisted fluidization” designs to supply extra energies or actuators to the system [1,5]. Assistance approaches classify based on the routes of manipulation - imposing dynamic or geometrical constraints on either gas or solid phase - and the modifications to forces, namely through a contact force (e.g., particle–particle and particle–wall), a surface force (e.g., particle–fluid) or a body force (e.g., external force fields and gravitational pull) [6]. Among various approaches, the external actuators, including vibration [3,7], pulsation [8], stirrer mixing [9], high-speed flow of jets [10–12], and adding flow conditioners [13–15], are currently prevalent and considered industrially relevant. Several successful attempts to enhance fluidization using these external actuators have been reported in the literature [2]. Nevertheless, there is not yet a universal approach to manipulate and attain the desired fluidization for cohesive powders. Complexity arises from the types of cohesion, scalability, energy consumption, and instrumentation.

In particular, the use of mechanical vibration to enhance fluidization of cohesive powders has attracted immense attention in the community [2]. Periodic oscillation of system boundaries agitates particles and, therefore, alters hydrodynamics through the momentum exchange

* Corresponding authors.
E-mail addresses: K.Wu-3@tudelft.nl (K. Wu), J.R.vanOmmen@tudelft.nl (J.R. van Ommen).

https://doi.org/10.1016/j.cej.2023.143936
Received 24 March 2023; Received in revised form 30 May 2023; Accepted 3 June 2023
Available online 5 June 2023

Nomenclature

ΔP	measured pressure drop, (mbar)
ΔP_0	theoretical pressure drop, (mbar)
μ	attenuation coefficient, (-)
σ	variation of gas fraction, (-)
ε	normalised gas fraction, (-)
A	vibration amplitude, (mm)
A_B	bubble area, (cm^2)
D	inner column diameter, (cm)
d	material thickness, (cm)
D_{32}	Sauter mean diameter, (μm)
D_{eq}	equivalent bubble diameter, (cm)
f	vibration frequency, (Hz)
H	bed height, (cm)
H_0	static bed height, (cm)
I	X-ray intensity on the detector, (-)
I_0	X-ray intensity from the source, (-)
I_{empty}	X-ray intensity of empty reference, (-)
I_{full}	X-ray intensity of full reference, (-)
$N_{\Delta t}$	number of frames over a chosen time interval, (-)
t	flow time, (s)
U_{mf}	minimum fluidization velocity, (cm/s)
X	horizontal position, (cm)
Y	vertical position, (cm)

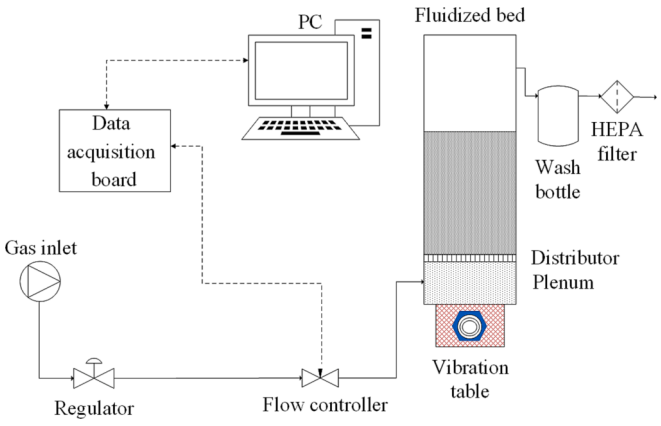

Fig. 1. Schematic representation of the experimental setup.

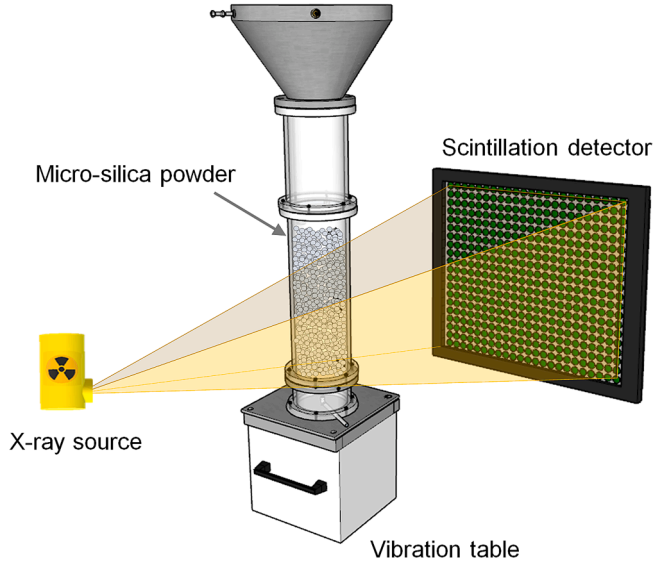

Fig. 2. Schematic representation of the X-ray imaging setup. The column is placed in between the X-ray source and detector.

between the particle-boundary contacts, such as between particles and distributor plate or side walls. Studies have been conducted to characterize the improvement induced by vibration, and shown the impacts of effective disruption on agglomerates [16] as well as gas channels [7,17,18], leading to a more homogeneous flow, bed expansion [19],

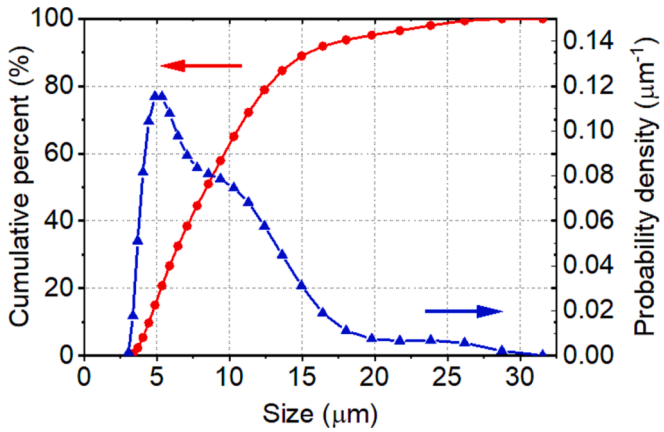

Fig. 3. Volume-based particle size distribution and cumulative distribution of the silica powder. Sauter mean diameter D_{32} is 7.9 μm.

reduced bubble size [20], reduced minimum fluidization velocity [21], and mitigated powder stratification [22]. Similar impacts are also witnessed for the fluidization of ultra-fine cohesive powders [23,24]. With several successful attempts, vibration assistance has been piloted in industrially relevant applications, such as aeration drying and conveying of cohesive powders [25–27]. Despite the improved fluidization witnessed, the studies conducted are largely limited to the observation on bulk response - bed expansion and pressure drop - and ex-situ analysis of agglomerates after fluidization [3,28,29]. Nevertheless, without understanding the flow behavior, measurement results are often perceived under the assumption of homogeneous fluidization. In fact, complex flow pattern and local structure of cohesive powders bias largely the measurements of bulk properties [13], and complicate the selection of representative sampling. Inspection of the bubbling behavior is limited to a relatively small transparent column (e.g., a diameter smaller than 3 cm), and the fluidization must be interpreted with extra concerns of significant boundary effects. Additionally, wall sheeting of powders occurs rapidly, significantly reducing visibility. Therefore, the fundamental physics and hydrodynamics induced are yet far from being understood, which substantially complicates relevant design, implementation, and scale-up practices [30].

Non-intrusive imaging and tomography techniques commonly used for medical and technical practices, such as electrical capacitance tomography [31,32], magnetic resonance imaging [33,34], and X-ray computational tomography (XRT) [35], provide opportunities for direct visualization and insights into system hydrodynamics [36]. In the literature, XRT has been successfully used to study the gas–solid fluidization of different powders [37] and geometries [38,39]. Based on the attenuation of X-ray beams by the local structure of gas–solid

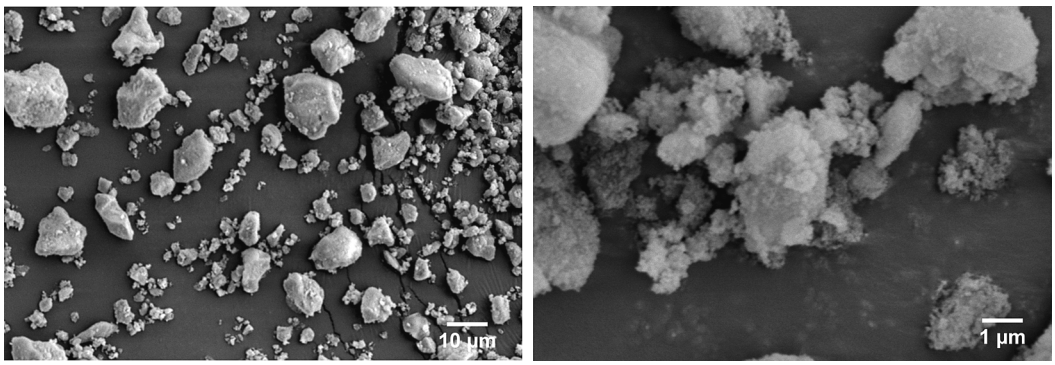

Fig. 4. SEM images of un-fluidized micron-silica powder.

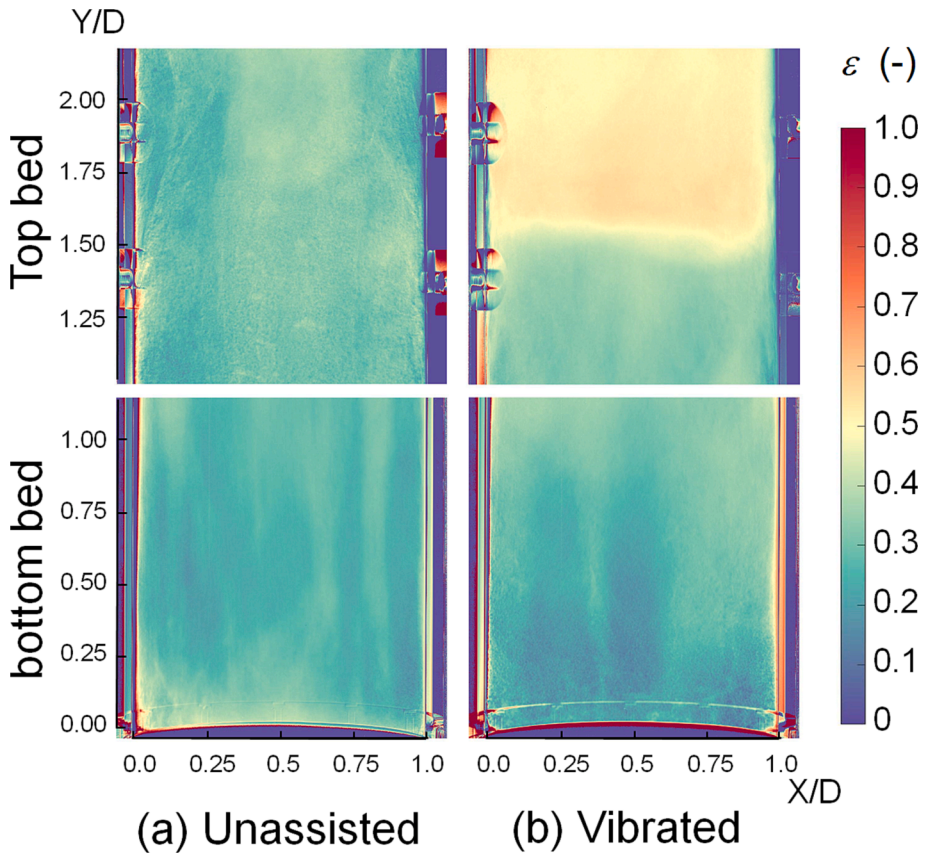

Fig. 5. Comparison of flow patterns in between (a) the unassisted and (b) vibro-fluidized beds. The flow patterns are obtained by averaging 20 s of frames captured 360 s after the fluidization process begins. $U = 1.8$ cm/s; $f = 30$ Hz; $A = 1.0$ mm. (see Supplementary Material for a video clip of the flow patterns).

suspension, a time-resolved flow pattern of fluidization is attainable, and the occurrence of local hydrodynamic events, such as bubble motion [40], gas channel breakage [41], bubble eruption [42], particle circulation [43] and transition between different flow regimes [44], can be monitored in a larger three-dimensional (3D) cylindrical column.

In this study, we experimentally investigate and compare the fluidization behavior of cohesive micron-silica in a cylindrical column with no-assistance and vertical mechanical vibration of varying strength. Two-dimensional (2D) projection fast X-ray imaging measurements are conducted, alongside pressure drop and bed expansion measurement, to capture and analyze the spatiotemporal evolution of flow patterns and identify in-situ hydrodynamic events, such as powder segregation, gas bubble and channel development. Increased vibration strength enhances the initialization of fluidization, and lowers the channel breaking velocity, whereas adjustment of vibration amplitude or frequency yields distinctive flow patterns and temporal development of fluidization. These results help optimize and design efficient vibro-assisted units for solid processing, and also provide opportunities for validation of the computational fluid dynamics codes for modelling fluidization behavior of cohesive powder.

2. Experimentation and methodology

2.1. Experimental setup

Fig. 1 shows a schematic representation of the experimental setup. The experiments are conducted using a Plexiglas column of 19.2 cm inner diameter. The unit couples to a plenum chamber beneath using a 3 mm thick, porous plate (SIKA-R 3 AX, Sintertech), with a classification of 3.3 μm grade efficiency. The porous plate is cleaned using an

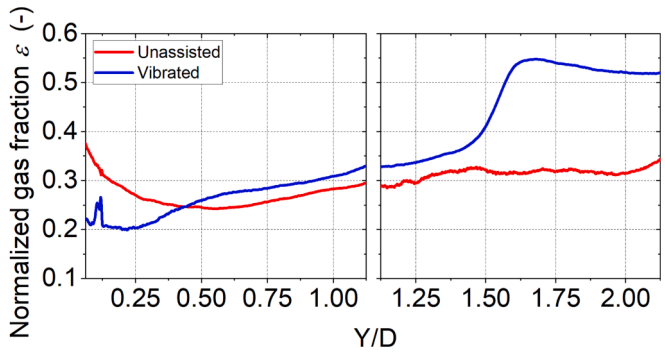

Fig. 6. Space-averaged gas fraction profiles in the vibrated and unassisted beds captured 360 s after the fluidization process begins. The profiles are obtained by averaging 10 s of frames. $U = 1.8$ cm/s; $f = 30$ Hz; $A = 1.0$ mm. The small peak at $Y = 0.12$ D is due to the misalignment of Perspex flanges during vibration.

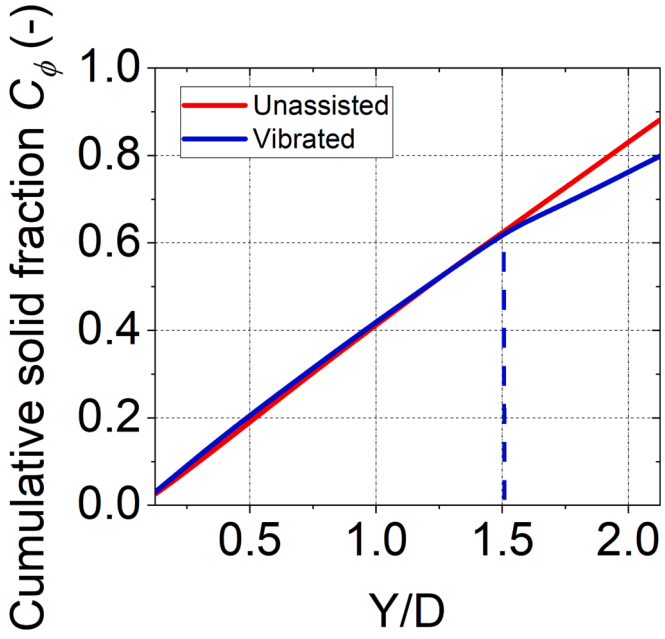

Fig. 7. Cumulative distribution of solid fraction C_ϕ in both the vibrated and unassisted bed captured 360 s after the fluidization process begins. The plot is computed based on the gas fraction in Fig. 6 using Eq. (9). $U = 1.8$ cm/s; $f = 30$ Hz; $A = 1.0$ mm.

ultrasound bath before use, and the plenum chamber is observed consistently free of particles after each experiment. An expansion breakout box is installed on top of the column to recycle entrained powders. Escaped particles are collected downstream using a wash bottle and a solid filter (HEPA) before releasing the fluidizing gas into the atmosphere. The column is mounted onto a vibration table, which allows vertical oscillation at the selected amplitude and frequency. The powders are fluidized at ambient temperature with a compressed, dry nitrogen gas flow manipulated by a mass flow controller (Bronkhorst F-202AV) at 4 bar. The flow controller and pressure transducers are connected to a data acquisition system controlled via an in-house LabVIEW panel. An optical camera positioned in front of the system records the bed expansion.

2.2. X-ray image processing

Fast X-ray imaging is a non-invasive and hard field technique to capture system hydrodynamics. X-ray beams are not deflected by the gas–solid suspension, but X-ray transmission is attenuated based on the mass of solids present in the field lines [35]. For each experiment, the attenuation of X-ray beams is measured at the detector panel to obtain 2D projected intensity maps of the field of view. The column is placed in between an X-ray generation tube and a detector panel, as shown in Fig. 2. The attenuation follows Lambert-Beer law:

$$I = I_0 \exp(-\mu d) \tag{1}$$

where I_0 and I are the intensity of X-ray beams before and after penetrating loaded material of a thickness d, μ is the attenuation coefficient associated with the material properties.

Thereby, X-ray attenuation measured on the scintillation detector portrays the spatial profile of gas fraction. The normalized gas fraction ε (referred to as gas fraction for simplicity in the following text) can be computed based on the two-point calibration protocol given two reference profiles of X-ray intensity:

I_{empty} for an empty column, and I_{full} for a fully loaded column, where, in the present study, the loaded powders are vibrated in prior for 10 min to approach a close packing. The gas fraction ε of the projection is calculated as follows:

$$\varepsilon(I) = \frac{\log\left(I/I_{full}\right)}{\log\left(I_{\text{empty}}/I_{\text{full}}\right)} \tag{2}$$

Note that the range of ε based on the definition is between 0 and 1, representing the close packing of the solids and pure gas, respectively. This range can be rescaled if the absolute gas fraction at the point of close packing is determined. For the gas fraction maps shown in the following text, low attenuation of X-rays is represented by reddish colors and indicates low solid concentrations. In contrast, high attenuation of X-rays is represented by dark blue colors and indicates high solid concentrations. The raw images are acquired at a frame rate of 22 Hz, which is considered sufficient to track the hydrodynamics. The X-ray imaging measurement focuses on sections of two different heights: the bottom bed view focuses on the area above the distributor plate, monitoring the surface of the distributor plate such as roots of channels, and the top bed view focuses on the field of view 225 mm above. Each field of view is 230 mm × 230 mm, and the detector pixel array consists of 1548 pixels × 1524 pixels, which results in a resolution of 0.15 mm/pixel. It is worth noting that the top and bottom views cannot be monitored simultaneously due to the detector size. Therefore, the two regions are inspected in sequence of independent experimental runs under the same conditions. The exact spatial gas–solid distribution, such as the location (horizontal position X and vertical position Y in the 2D projection) of gas channels and bubbles, may be different, but one should expect reproducible bulk profiles. Further details of the setup used have been demonstrated in the work of Maurer et al. [38].

2.3. Powder properties

Commercially available Geldart C Silica powder (CWK Bad Köstritz) is used in this study. The measurement of laser diffraction particle analyzer exhibits a mono-peak size distribution characterized by a Sauter mean diameter of 7.9 μm, as shown in Fig. 3. The size distribution agrees with the image analysis from optical microscopy. The cohesive silica powder tends to form agglomerates when closely in contact. A few loosely bonded grains already form primary agglomerates prior to fluidization. The scanning electron microscopy (SEM) images of the fresh powder indicate the presence of primary agglomerates, shown in Fig. 4, which are highly complex in shape. The silica powder is porous with a density of 1900 kg/m^3. Its theoretical minimum fluidization velocity U_{mf} is calculated as 0.002 cm/s according to the Gidaspow correlation [45]. However, our preliminary test shows that the powder bed remains channeling up to 7 cm/s, making the determination of the experimental U_{mf} impractical. The powders behave fluffy, and the bulk density is 145 kg/m^3 determined by filling a measuring column without

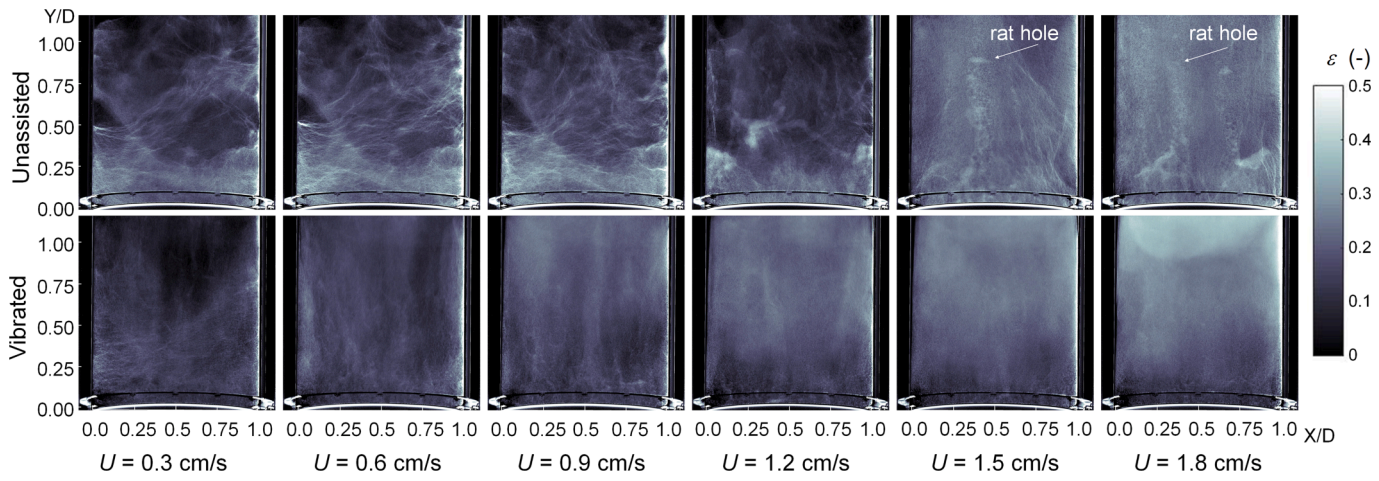

Fig. 8. Time-averaged flow patterns at elevated velocities in the lower part of vibrated and unassisted beds. The bed is fluidized continuously over the entire process of increasing the gas velocity. Each flow pattern is obtained by averaging 10 s of frames captured 360 s after the fluidization process begins. Blurred areas indicate more hydrodynamic events, such as moving particles or bubbles. $U = 1.8$ cm/s; $f = 30$ Hz; $A = 1.0$ mm. The contrast is enhanced by using a dark-blue color scheme. Note the scale of the color bar.

consolidation. The dynamic angle of repose is measured as 50° at 30 revolutions per minute, indicating a poor flowability according to Carr's classification [46]. For the fluidization experiments, 1403 g powder is loaded, constituting a bed height of about 33 cm ($H_0/D = 1.65$).

2.4. Pressure measurement

Pressure drop over the entire fluidized powder bed is measured continuously to assist in evaluating the quality of fluidization. The pressure oscillation is collected at 1000 Hz, in order to minimize the noise influence. The driven oscillations of bed mass and gas created by both periodic vertical vibration and rising bubbles are reflected in the time series of pressure. However, the former is much more significant than the contribution imposed by the latter. To further distinguish the components, the signals are analyzed in both time and frequency domain, depicted in time-averaged and power-spectrum plots [47,48]. In particular, time-averaged pressure drop is commonly used to assess fluidization, while its standard deviation, mainly associated with vibration in the current scenario, is therefore discarded. For a bed height of 33 cm, the natural frequency of the powder bed is computed to be 1.7 Hz using the formulation provided by Baskakov et al. [49]. Besides, for fluidization, the occurrence of dominant hydrodynamic events is observed at frequencies lower than 10 Hz [47], and the oscillations at much higher frequencies are considered induced by the system or vibration.

2.5. Mechanical vibration

The column is vibrated vertically at frequencies up to 30 Hz and amplitudes up to 2 mm, with the consideration of device operation and mechanical capability of further scale-up practices. For an ideal sinusoidal oscillation, vibration strength is commonly characterized by a dimensionless Froude number Γ, defined as the ratio of maximum driving acceleration over the gravitational acceleration [50]:

$$\Gamma = \frac{A(2\pi f)^2}{g} \tag{3}$$

where A is the vibration amplitude, f is the vibration frequency, and g is the gravitational acceleration. The vibration created is calibrated using a high-speed camera (Olympus i-speed 2) recording at 1000 frame per second, and shows a decent sinusoidal oscillation based on image analysis.

2.6. Bubble detection

For a 2D projection of the flow pattern, a bubble is defined as the area consisting of pixels where the gas fraction exceeds a threshold determined from the surroundings. Bubble identification is carried out after 360 s of fluidization to ensure a steady-state, and samples over 60 s, that is 1220 frames in total, for each experiment. An in-house MATLAB code is used to capture the bubbles by adaptive thresholding [51]. The equivalent bubble diameter D_{eq} is calculated from the bubble area A_b:

$$D_{eq} = \sqrt{\frac{4A_b}{\pi}} \tag{4}$$

The minimum area of bubbles extracted is set to 2000 pixels of the X-ray view of focus, equivalent to a diameter of 7 mm, to remove spurious bubbles.

2.7. Flow pattern and variability

With the gas fraction ε obtained from the X-ray imaging, a time-averaged gas fraction profile ε can be computed as follows:

$$\overline{\varepsilon}(x,y) = \frac{1}{N_{\Delta t}} \sum_{t=t_0}^{t_0+\Delta t} \varepsilon(x,y,t) \tag{5}$$

where $N_{\Delta t}$ is the number of X-ray imaging frames between t_0 and $t_0 + \Delta t$, x and y are the horizontal and vertical positions.

Besides, the standard deviation of the gas fraction indicates the flow pattern variability in time. Alongside the horizontal direction, an instantaneous line- averaged gas fraction is obtained for each flow time t, and the time-based standard deviation of a line-averaged gas fraction σ_y at a flow time t can be calculated:

$$\overline{\varepsilon}_y(y,t) = \frac{1}{N} \sum_{x=1}^{N} \varepsilon(x,y,t) \tag{6}$$

$$\overline{\overline{\varepsilon}}_y(y) = \frac{1}{N_{\Delta t}} \sum_{t=t_0}^{t_0+\Delta t} \overline{\varepsilon}_y(y,t) \tag{7}$$

$$\sigma_y(y) = \sqrt{\frac{\sum_{t=t_0}^{t_0+\Delta t} \left[\overline{\varepsilon}_y(y,t) - \overline{\overline{\varepsilon}}_y(y)\right]^2}{N_{\Delta t} - 1}} \tag{8}$$

where $\overline{\varepsilon}_y$ is the horizontal line-averaged gas fraction, $\overline{\overline{\varepsilon}}_y$ is the time-

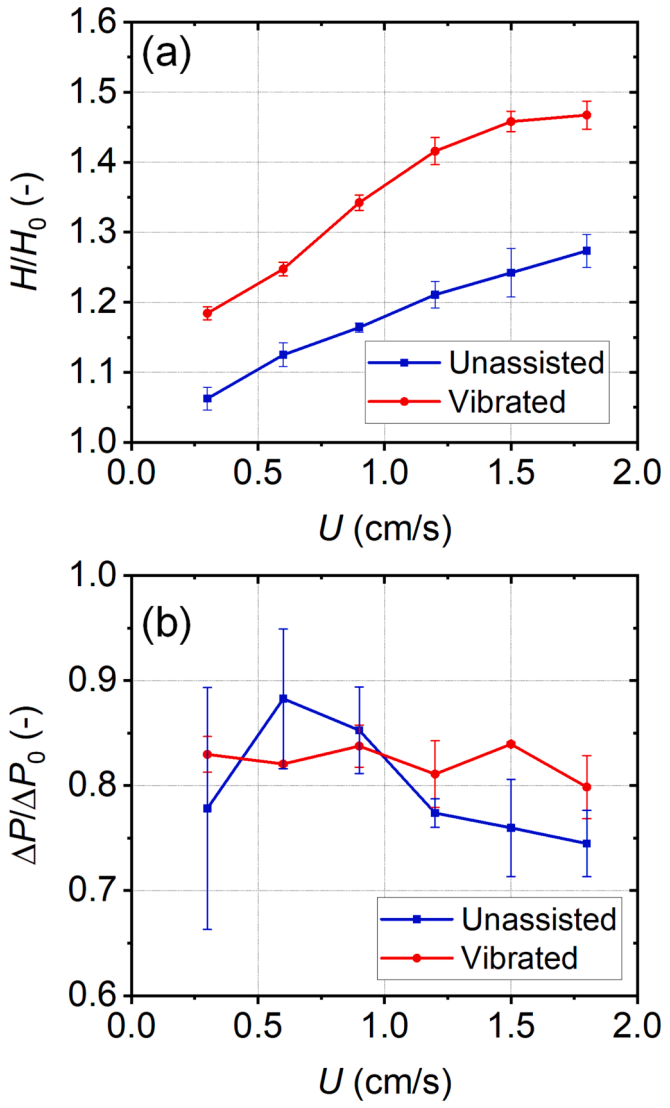

Fig. 9. (a) Bed expansion and (b) normalized pressure drop in both unassisted and vibrated beds at increasing gas velocities from 0.3 cm/s to 1.8 cm/s. The theoretical pressure drop at complete fluidization, $\Delta P_0 = 4.83$ mbar, is used for normalization. The error bars stand for reproducibility from three experiments. Each experiment was carried out separately when changing the gas velocity. The data were captured 360 s after the fluidization process begins.

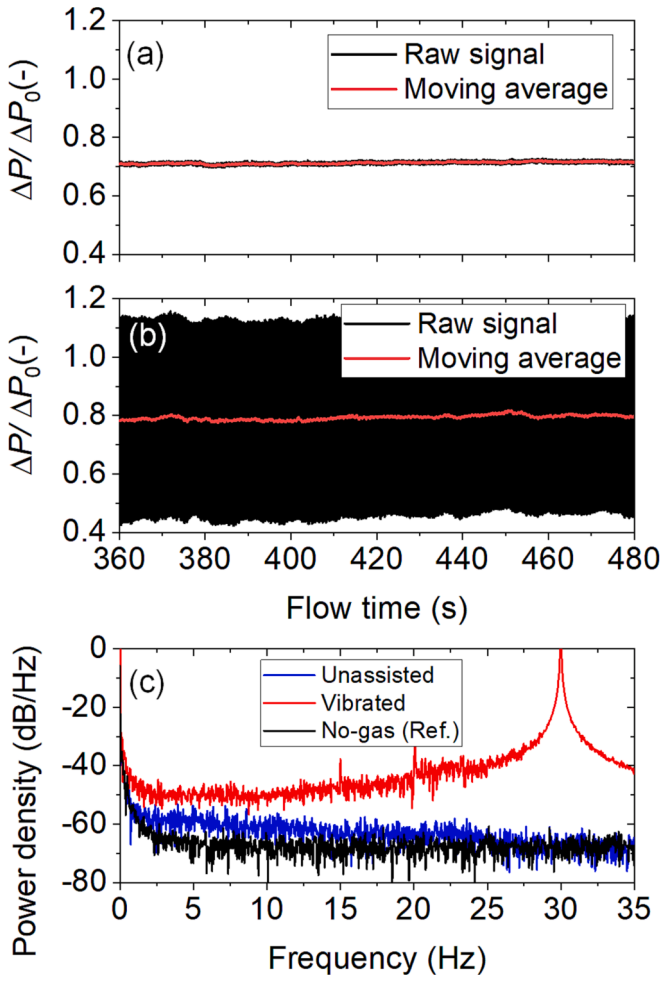

Fig. 10. Time series of bed pressure drop in the (a) unassisted and (b) vibrated beds, and (c) the associated power spectrum. The signals are sampled 360 s after the fluidization process begins. $U = 1.8$ cm/s; $f = 30$ Hz; $A = 1.0$ mm.

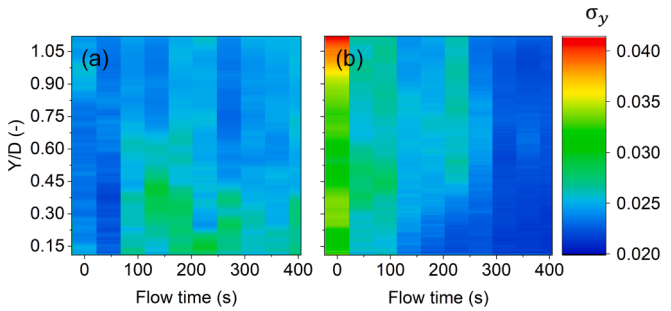

Fig. 11. System variability in the bottom section for both (a) the unassisted and (b) vibrated beds. The standard deviation σ_y is computed at each chosen time with a time interval $\Delta t = 20$ s. $U = 1.8$ cm/s; $f = 30$ Hz; $A = 1.0$ mm.

averaged of $\bar{\varepsilon}_y$. Low values of σ_y represent regions with less or no bubbling or movement of solids. Regions with frequent bubbles and solid motion give rise to a large σ_y. Therefore, σ_y can be considered as a quantitative indication for the system variability within a time interval.

3. Results and discussion

To thoroughly identify and investigate the effects of mechanical vibration, experiments of different vibration conditions and superficial gas velocities have been conducted, and the resulted flow behavior are compared to the ones of unassisted fluidization. In this section, a comprehensive comparison between the unassisted and vibro-fluidization is presented and studied in terms of flow patterns, stability, solid distribution, pressure drop and bed expansion. Subsequently, the influences of vibration frequency and amplitude on the flow behavior are discussed.

3.1. Hydrodynamics of the unassisted and vibro-fluidized bed

Unassisted and vibro-fluidization of cohesive powder differ significantly in flow patterns. When subjected to dry nitrogen gas, the micron-silica powders, without assistance, initially bond together and rise as a plug. At a certain height, this plug collapses, and the lifted powders progressively fall and settle back onto the distributor plate, creating a slightly dilated bed with internal cracks. In contrast, vibration (e.g., $f =$ 30 Hz, $A = 0.5$ mm) suppresses the formation of such a powder plug, but

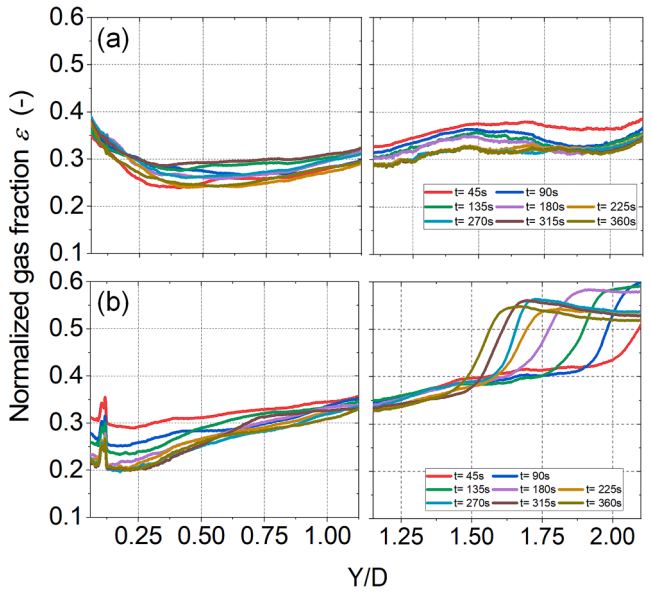

Fig. 12. Temporal evolution of axial gas fraction in both (a) the unassisted and (b) vibro-fluidized beds. The gas fraction is obtained averaging 10 s of frames after the time chosen. $U = 1.8$ cm/s; $f = 30$ Hz; $A = 1.0$ mm.

Table 1
Experimental conditions investigated.

Set	Vibration conditions		
	Frequency f [Hz]	Amplitude A [mm]	Strength Γ [-]
1	10, 20, 30	1.0	0.4, 1.6, 3.6
2	10	0.5, 1.0, 1.5, 2.0	0.2, 0.4, 0.6, 0.8

dilates the bed rapidly with the fluidizing gas, in a similar fashion to fluidization of Geldart A particles.

Fig. 5 compares the steady-state flow patterns attained 360 s after the fluidization process begins at $U = 1.8$ cm/s. Without any external assistance, the powders yet remain largely stationary under the fluidizing gas. Channels stem from the distributor plate, and merge throughout the bed. In particular, these gas channels are initially evenly distributed in the area near the distributor plate, but slowly relocate over time. Therefore, a slight expansion is expected. In the top bed, multiple tube-like channels of roughly 1 cm wide approach each other and coalesce into a massive "rat hole", located in the bed center, as shown in Fig. 5a, which allows for fast rising bubbles to travel inside. These channels break up in proximity to the bed surface, output gas in a jet-like manner and result in intense, local oscillations of the bed surface.

On the other hand, mechanical vibration facilitates fluidization, yet not equally effective to all height Y in the bed. Three different flow regions develop over time under vibration, which are denoted here as the stagnant regime, dense regime and dilute regime. Fig. 5b depicts a $Y \leq 0.4D$ dense layer of powders deposited onto the distributor plate without being recirculated, which coincides with the region of channels nucleation in the unassisted bed. Differently, local bubbles in the vibro-bed emerge on the surface of the dense layer (e.g., around $Y/D = 0.4$, as can be seen from Fig. 5 and its video clip in Supplementary Material) instead of emerging from the distributor plate. In addition, the internal structure of gas–solid suspensions is unstable and evolves over time. Subsequent to an initial expansion, a sharp interface forms at the top bed, separating two distinct regions, and progressively descends throughout the bed. Intensive fast bubbling takes place above this interface, driving rapid powder circulations and intense agitation of the top surface, whereas only local streams of bubble appear in the region right underneath the interface, qualitatively similar to gas channeling.

Separation of different regimes can also be seen in the axial profile of gas fraction. Fig. 6 displays a 15 % difference in the gas fraction for the region above the distributor plate ($Y/D \leq 0.4$) after 360 s fluidization between the two systems, in which gas channels arise and dilate the unassisted bed, whereas solids compact and become stagnant in the vibrated bed. For the unassisted bed, the gas fraction ε quickly reduces from 0.4 to 0.25, due to the immediate coalescence of gas channels, and then almost plateaus, as these channels align and expand axially throughout the bed without interfering with the surrounding solids. In contrast, ε in the vibrated bed surpasses the unassisted bed from $Y = 0.4D$ onwards with the emergence of local gas bubble streams. A sharp increment in ε, from 0.35 to 0.55, designates the separation of dilute and dense regimes at around $Y = 1.5D$, as shown in Fig. 6. Therefore, it is convenient to distinguish three regimes in the vibro-beds: the stagnant regime in the bottom bed, as well as the dense and dilute regimes separated by a sharp interface in ε. Based on the axial gas fraction, a cumulative solid fraction distribution C_ϕ can be obtained via the gas fraction distribution:

$$C_\phi(y) = \frac{\sum_{y=1}^{y}\left[1-\overline{\overline{\varepsilon}}_y(y)\right]}{\sum_{y=1}^{H_0}\left[1-\overline{\overline{\varepsilon}}_{H_0,y}(y)\right]} \tag{9}$$

where $\overline{\overline{\varepsilon}}_{H_0,y}$ is the gas fraction measured before fluidization, and H_0 is the initial bed height. According to the cumulative fraction distribution shown in Fig. 7, 60 % of the total mass hold-up is located beneath the interface, remaining only partially fluidized. A clear separation between the two curves starts at $Y = 1.5D$, which corresponds to the interface between the dilute and dense regimes in the vibro-bed.

Fig. 8 displays the time-averaged flow patterns at elevated gas velocities. The bed is fluidized continuously over the entire process of an intermittently increased gas velocity, in order to capture the proceeding development of internal cracks and gas channels. At each velocity, the fluidization is maintained for 360 s to ensure a steady state. In unassisted beds, cracks, the precursor of gas channels, stem from the distributor plate at low velocities (e.g., $U \leq 0.3$ cm/s), and stabilize as groups of non-bubbling vein-like branches concentrated at $Y \leq 0.5D$. Instead of shooting axially throughout the bed, these cracks curve and grow diagonally. As the flow rate is increased, they self-arrange from curved, micro-cracks into axial, macro-gas channels, and merge into larger tubes at a higher distance from the distributor plate. Such a transition occurs at $U = 1.2$ cm/s, where the vein-like cracks hardly withstand the increased gas throughput and rupture (see Supplementary Material for the channel transition process). Under higher gas velocities, neighboring channels gradually merge to form a "rat hole" (from $X/D = 0.25$ to 0.4). At this stage, the fluidizing gas largely bypasses the bed.

Vibration destabilizes gas channels and promotes bubbling. Vertical vibration constantly decouples loosely bonded powder and allows for gas to enter interstitial gaps, and Fig. 8 shows that much slender cracks appear and stagger horizontally at low gas velocities. As the velocity is increased to $U = 0.6$ cm/s, staggered micro-cracks break up and release bubbles. Such a vibration also facilitates powder stratification. It is observed that activated particles, as well as agglomerates of larger size, travel downwards continuously under the vibration, forming a stagnant region consisting of micro-channels, as aforementioned. The height of the stagnant region progressively grows with increasing gas velocity, and the particles within compact and remain stagnant, functioning as "a secondary distributor". Simultaneously, as the gas velocity increases, bubbles arise increasingly from the surface of the stagnant region (around $Y/D = 0.4$). Both vigorous bubbling and increased gas velocity enhance the separation of the dilute and dense regions, by promoting particle circulation and agitation of the top bed. As the velocity is increased to $U = 1.8$ cm/s, the interface descends and becomes visible in the bottom bed, at $Y = 0.9D$.

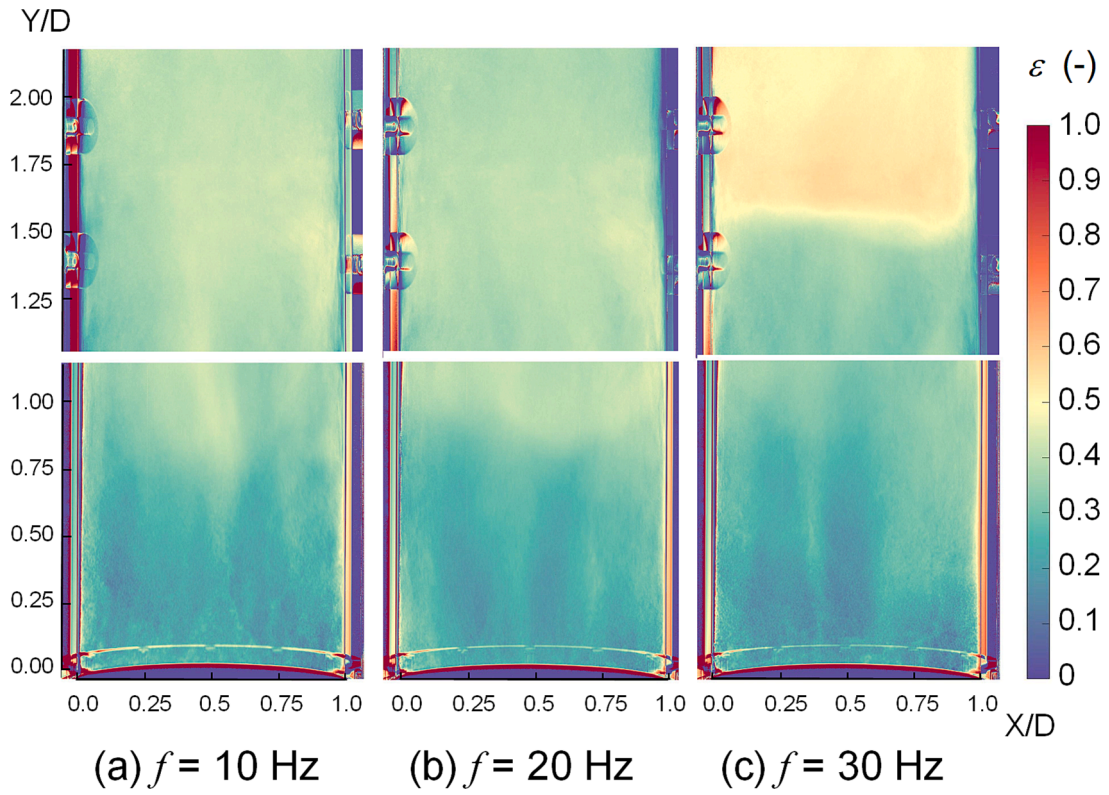

Fig. 13. Time-averaged flow patterns in the vibro-fluidized beds of varying frequency f = (a) 10, (b) 20 and (c) 30 Hz under an amplitude of 1 mm (corresponding to Γ = 0.4, 1.6 and 3.6) The flow patterns are obtained by averaging 20 s of frames captured 360 s after the fluidization process begins. U = 1.8 cm/s.(see Supplementary Material for a video clip of the flow patterns).

3.2. Bed expansion and pressure drop

The silica powder dilates more significantly with increasing gas velocity when applying vibration. The comparison in Fig. 9a shows the bed expansion of varying gas velocities. Vibration greatly collapses those persistent channels, and assists in dilating the bed because of enhanced inter-phase contacts.

However, the occurrence of stratification depresses the overall bed expansion over time. On the other hand, much lower expansion observed in the unassisted beds is attributed to the excessive gas bypass. Gas channels occur from U = 1.2 cm/s, and spout powders, creating an uneven bed surface. Within the velocity range tested, the vibro-beds achieve 15–20 % higher bed expansion in comparison to the unassisted beds.

Due to the inhomogeneous flow structure of gas–solid mixture, it is challenging to evaluate the fluidization of cohesive powder based on the time-averaged pressure drop ΔP over the theoretical pressure drop at complete fluidization ΔP_0. Fig. 9b shows that both the unassisted and vibro-bed exhibit $\Delta P/\Delta P_0 \geq 0.7$, however, the corresponding hydrodynamics differ greatly. The pressure drop for the unassisted bed relies upon the internal structure. The cracks created at low gas velocities are distributed inside the bed, allowing for decent gas–solid contacts, but they form chaotically and are associated with the initial packing, which varies the measured pressure drop significantly. When these cracks evolve into gas channels at higher velocities, the gas-bypass depresses the inter-phase contact, lowering the total pressure drop. The reduction in pressure drop is attributed to the enlargement of gas channel size from U = 1.2 cm/s to 1.8 cm/s. Based on the flow patterns shown in Fig. 8, the pressure drop in a vibro-bed consists of three parts: contribution by packed solids in the stagnant region, channels in the dense region, and suspension of solids in the dilute region. Powders inside the stagnant region compact firmly, functioning as a “secondary distribution plate”. Besides, Fig. 8 suggests that only the particles in the dilute region are effectively suspended, which is much less than 80 % of the total hold-up indicated by $\Delta P/\Delta P_0$.

The range of the pressure fluctuations of the unassisted beds remains lower than 3 %, while the vibration of interstitial gas and solid mass induces around 50 % deviation, as shown in the time-series plots Fig. 10a and b. The power spectrum demonstrates that the maximum intensity is located at f = 30 Hz, therefore the large oscillation in the pressure drop series is mainly driven by the external vibration. By focusing on the low frequency region ($f \leq$ 10 Hz), orders of magnitude higher intensities are observed in the vibro-bed, meaning more dynamic events occur in the bed. Overall, the time-averaged pressure drop is not ideal for evaluating the fluidization state of the cohesive powder, and tend to overestimate the effectiveness of solids fluidization, whereas the power-spectrum seems to provide more insights into the quality of fluidization.

3.3. Temporal evolution and stability of flow pattern

The fluidization process of cohesive powder evolves over time, following the initial bed expansion. Fig. 11 demonstrates the variability of local structures over time at U = 1.8 cm/s. The calculation is demonstrated in Section 2.7, and only the pixels between the inner walls are considered. In the unassisted bed, channels form immediately once the plugging powder settles. Gas bubbles emerge from the distributor plate and continuously travel within the channels, resulting in poor fluidization. At such a gas velocity, the internal structure is unstable and alternates between the forms of multiple tube-like channels and few rat holes. Fig. 11a shows the channel structure yet continues to evolve after 360 s of fluidization, and varies more frequently in the region close to the distributor plate ($\sigma_y \geq 0.04$). In contrast, once the vibration begins, the bed initializes with a rapid expansion ($\sigma_y \geq 0.05$), as shown at 0 s in Fig. 11b, and gradually develops different regimes. Powders and agglomerates of large size settle down to develop the stagnant and dense

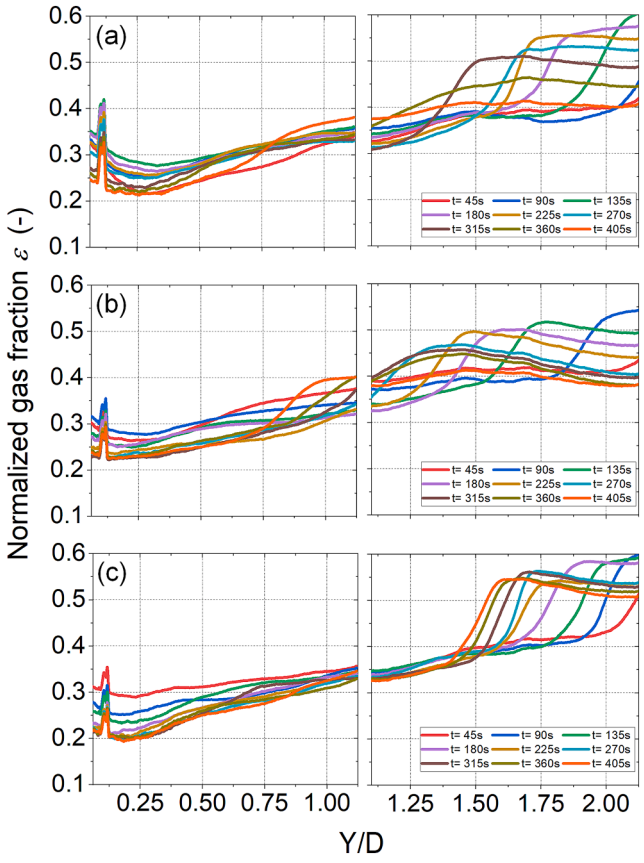

Fig. 14. Temporal evolution of axial gas fraction in the vibro-fluidized beds of varying frequency f = (a) 10, (b) 20 and (c) 30 Hz under an amplitude of 1 mm (corresponding to Γ = 0.4, 1.6 and 3.6). The gas fractions are obtained by averaging 10 s of frames captured after each time chosen. U = 1.8 cm/s.

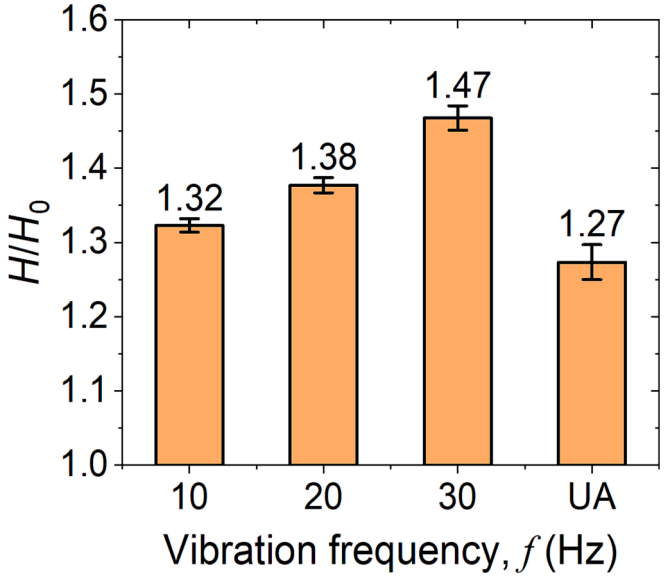

Fig. 15. Bed expansion in vibro-fluidized beds of varying frequency f = 10, 20 and 30 Hz under an amplitude of 1.0 mm (corresponding to Γ = 0.4, 1.6 and 3.6). Bed expansion in the unassisted bed (UA) is included as a reference. The bed heights are sampled at 360 s. U = 1.8 cm/s.

regions. In particular, the stagnant regime becomes recognizable from 100 s onwards, where the standard deviation is insignificant ($\sigma_y \leq 0.03$), and grows over time.

Fig. 12 compares the temporal axial gas fraction profiles. For the unassisted beds, the cluster of vein-like channels remains and

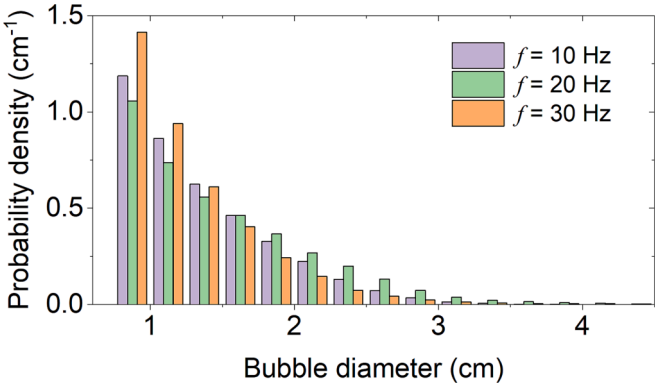

Fig. 16. Bubble size distribution in vibro-fluidized beds of varying frequency f = 10, 20 and 30 Hz under an amplitude of 1.0 mm (corresponding to Γ = 0.4, 1.6 and 3.6). The bubbles are sampled over 60 s of frames captured 360 s after the fluidization process begins. The distribution is obtained based on count. U = 1.8 cm/s.

Table 2
The effect of vibration frequency on gas bubbles. The amplitude is kept at A = 1 mm.

Frequency f	Equivalent bubble diameter		Bubble count
	By count (cm)	By area (cm)	[-]
10 Hz	1.22	2.28	54,923
20 Hz	1.31	3.07	49,781
30 Hz	1.12	1.93	80,284

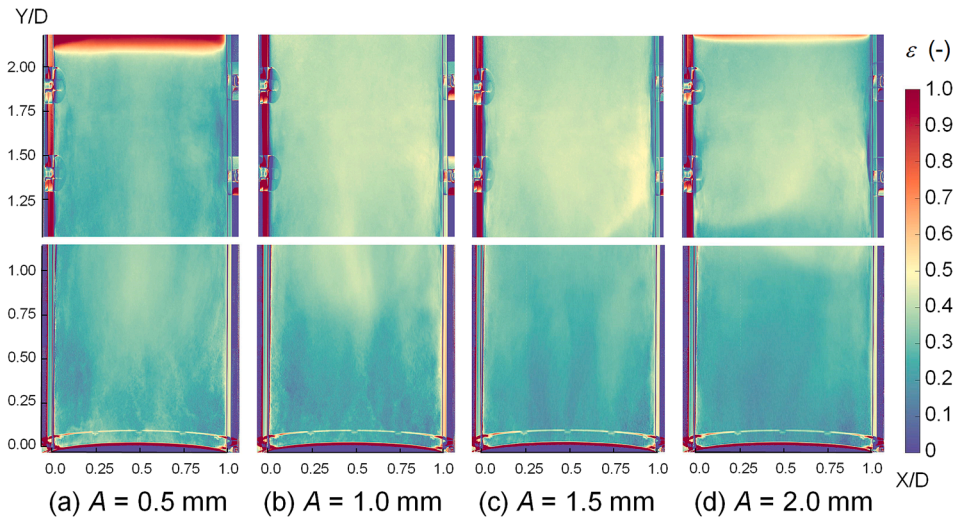

Fig. 17. Time-averaged flow patterns in the vibro-fluidized beds of varying amplitude A = (a) 0.5, (b) 1.0, (c) 1.5 and (d) 2.0 mm under a frequency of 10 Hz (corresponding to $\Gamma = 0.2$, 0.4, 0.6 and 0.8). The flow patterns are obtained by averaging 20 s of frames captured 360 s after the vibration process begins. $U = 1.8$ cm/s. (see Supplementary Material for a video clip of the flow patterns.).

contributes to the higher gas fraction in the bottom bed. The slight increase in the gas fraction in the top bed is attributed to the bursting of bubbles at the channel end, but both the gas fraction and amount of bubbles degrades over time. Above the cluster of channels, the gas fraction axial profile remains relatively constant throughout the bed around $\varepsilon = 0.3$, suggesting the formation of a steady internal structure. In contrast, the profiles of the vibrated beds illustrate the dynamic development of the three regions. Especially, the interface between dilute and dense regions, described by a steep increase in ε, starts from the top surface, and descends throughout the bed with reducing ε. Besides, the stagnant region in the bottom yet compacts increasingly with vibration, reducing to $\varepsilon = 0.2$ after 240 s.

3.4. Impact of vibration condition on hydrodynamics

Varying vibration strength, either via frequency or amplitude, is able to manipulate the fluidization behavior. Several studies adopted the concept of Γ to quantify the influence of vibration [25,28,52,53]. Nevertheless, one should expect different effects by varying frequency and amplitude independently. Table 1 lists the vibration conditions investigated.

3.5. Influence of vibration frequency

Fig. 13 displays the flow patterns of three different vibration frequencies, collected after 360 s, at the amplitude of 1 mm. For $f = 10$ Hz and $A = 1$ mm ($\Gamma = 0.4$), the stagnant region grows to around $Y = 0.25D$. Powders within the stagnant region develop micro-channels, allowing gas to bypass. At few centimeters higher than the stagnant region, bubbles emerge locally within larger gas channels, leading to the formation of a dense layer. The powder does not respond as swiftly as that at higher frequencies, and the existing channels only breakdown after 30 s of vibration. The gas fraction profiles shown in Fig. 14 point out that the stratification of dilute and dense region occurs and can be observed from 135 s after vibration. This stratification interface continuously descends and sits at $Y = 0.75D$ after 360 s. Simultaneously, both dilute and dense layers continue to compact over time, the stagnant layer intensifies towards a gas fraction of 0.2, and the dilute phase continues to decay with reducing ε. More bubbles are released on the interface, which also causes a broader shoulder in the profile. As the frequency is increased to 20 Hz, the dilation occurs more rapidly once the vibration starts.

The separation between dense and dilute layers emerges from 90 s at the top surface, propagating downwards gradually alongside the fluidization at a faster speed than at 10 Hz. Nevertheless, after 360 s, the interface also arrives at a height comparable to that observed at 10 Hz. With the presence of more rapidly rising bubbles, the powder is further suspended, resulting in an increased depth of the dilute region. Further increasing the vibration frequency to 30 Hz, the higher strength allows initializing the fluidization immediately, and renders the dilute region. At the beginning of vibration, the gas channels in the bottom rapidly collapse and burst into bubbles, and vanish later with the formation of a stagnant region. The separation interface also becomes visible from 45 s, but with a much larger bed expansion. Furthermore, the separation interface sinks more slowly, suggesting a superior characteristic of maintaining fluidization compared to the lower frequencies. After 405 s, the separation interface still sits around $Y = 1.5D$, nearly 50 % higher than at both 10 Hz and 20 Hz. The dilute region also exhibits less decay with ε maintaining above 0.5. However, the stagnant region condenses more significantly and rapidly at 30 Hz. Fig. 14 shows a stagnant compaction at ε of 0.20 developed in the bottom bed after 180 s, while the stagnant region is still compacting at 10 Hz and 20 Hz.

In general, the bed expansion increases with frequency. According to Figs. 13 and 14, gas–solid suspension is inhomogeneous, and the difference mainly lies on the depth of dilute regions. The bed expansion at 30 Hz is 10 % higher than at 10 Hz, which, however, cannot be directly translated into a 10 % improvement in fluidization, as shown in Fig. 15. Fig. 16 and Table 2 show the impact of vibration frequency on the equivalent bubble diameter D_{eq}. Bubbles are only determined in the top bed, as the bottom section consists of stagnant and dense regions, where mostly gas channels are present (see examples of captured bubbles in Supplementary Material). At $f = 30$ Hz, more tiny bubbles of $D_{eq} \leq 1$ cm have been created in the dilute regime, as shown in Fig. 14. These tiny, rapidly rising bubbles drive a significant circulation of solids, which further facilitates in maintaining the expansion of the dilute region. In addition, the stratification interface developed is not always flat, and, consequently, the rising bubbles arriving at the interface can be further redirected alongside the interface, leading to either a clockwise or counterclockwise bulk circulation of the solids. On the other hand, D_{eq} peaks at $f = 20$ Hz, given the dilute region in the top bed. These bubbles rise through the entire domain, resembling the fluidization of Geldart A and B particles, and no particular circulation pattern develops. When the frequency is reduced to $f = 10$ Hz, a similar flow of bubbles emerges, but with a slightly reduced bubble size. Besides, one could observe several

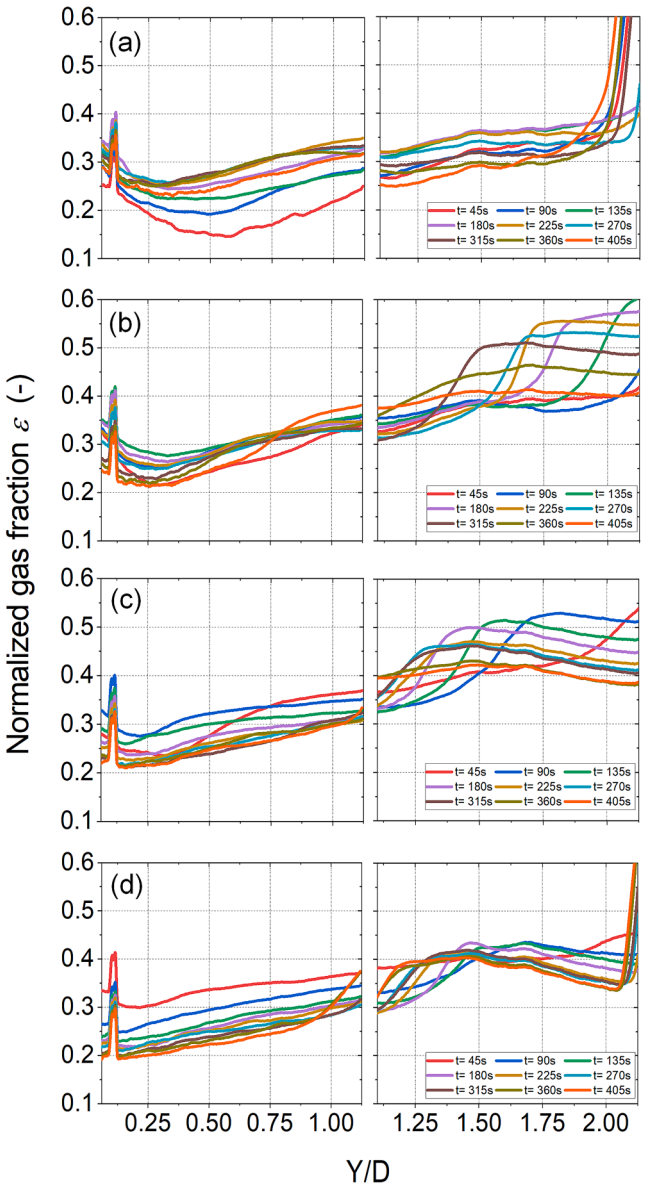

Fig. 18. Temporal evolution of axial gas fraction in the vibro-fluidized beds of varying amplitude A = (a) 0.5, (b) 1.0, (c) 1.5 and (d) 2.0 mm under a frequency of 30 Hz (corresponding to $\Gamma = 0.2$, 0.4, 0.6 and 0.8). The gas fractions are obtained by averaging 10 s of frames after each time chosen. $U = 1.8$ cm/s.

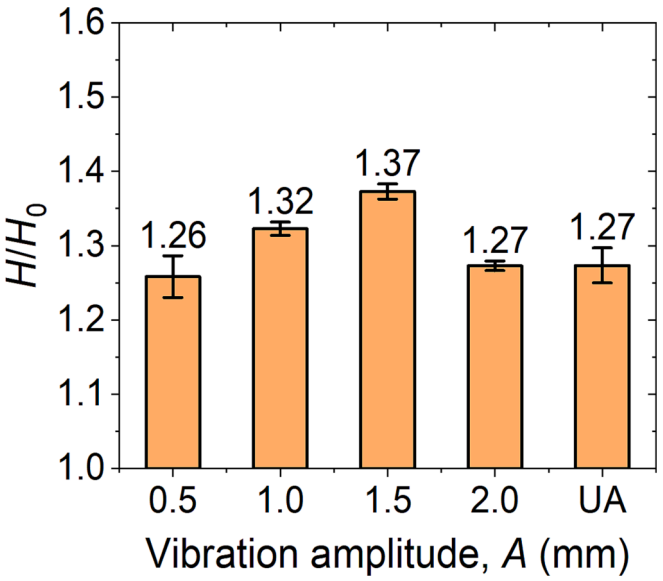

Fig. 19. Bed expansion in vibro-fluidized beds of amplitude $A = 0.5$, 1.0, 1.5 and 2.0 mm, at a frequency of 10 Hz (corresponding to $\Gamma = 0.2$, 0.4, 0.6 and 0.8). Bed expansion in the unassisted bed (UA) is included as a reference. The bed heights are sampled at 360 s. $U = 1.8$ cm/s.

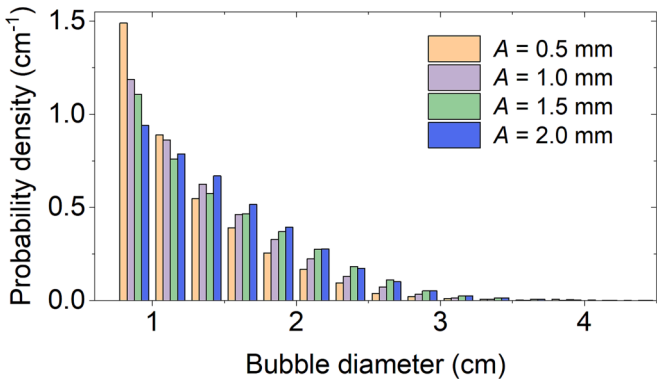

Fig. 20. Bubble size distribution in vibro-fluidized beds of varying amplitude $A = 0.5$, 1.0, 1.5 and 2.0 mm under a frequency of 10 Hz (corresponding to $\Gamma = 0.2$, 0.4, 0.6 and 0.8). The bubbles are sampled over 60 s of frames captured 360 s after the vibration process begins. The distribution is obtained based on count. $U = 1.8$ cm/s.

horizontal channel-like bubbles in the domain, due to the periodical vertical vibration.

Overall, a higher frequency is able to drive greater bed expansion of the dilute and dense region, but not necessarily better fluidization, whereas the stratification is expected to progressively develop and eventually lead to a similar flow pattern as for a lower frequency (e.g., $f = 10$ Hz). In addition, it is worth noting that these frequencies are away from the natural frequency (1.7 Hz), so the resonance effect is insignificant. Apparently, the results indicate that an increased frequency could improve the formation of the dilute region, but also compact the solids in the stagnant region. Nevertheless, it should be noted that vibration of a higher frequency is mechanically challenging for reactors of a large scale.

3.6. Influence of vibration amplitude

The impact of vibration amplitude on the bed hydrodynamics is investigated by keeping the vibration frequency unchanged at 10 Hz, while increasing the amplitude A from 0.5 mm to 2.0 mm. At $A = 0.5$ mm, only gas channels develop in the bottom bed alongside slight bubbling at the top bed. Such a low amplitude just slightly promotes bed expansion, and stratification is not observed after 360 s of fluidization, as shown in Fig. 17a and Fig. 18a. The bed responds slowly, and the expansion peaks at around 270 s, then rapidly degrades. At this stage, the vibration is not sufficiently large to collapse the channels formed in

Table 3
The effect of vibration amplitude on gas bubbles. The frequency is kept at $f = 10$ Hz.

Amplitude, A	Equivalent bubble diameter		Bubble count
	By count (cm)	By area (cm)	[-]
0.5 mm	1.11	2.01	49,723
1.0 mm	1.22	2.28	54,923
1.5 mm	1.28	2.75	51,687
2.0 mm	1.33	2.65	65,405

the bottom bed and induce effective fluidization. As the amplitude rises to 1.0 mm, the bed expands further and stratification of dilute and dense region appears, with homogeneous bubbling in the top bed. The fluidization evolves from channeling to mild bubbling. Further increasing the amplitude to 1.5 mm, the bed expands remarkably to $H = 1.36H_0$ with more significant bubbling, where the bed evolves from a mild fluidization state towards vigorous fluidization, where powders at the surface are agitated and erupt into the freeboard region due to the oscillation. The bed expansion increases proportionally with smaller amplitudes, but decreases at a larger amplitude. As the amplitude is increased to $A =$ 2.0 mm, the stratification takes place immediately with a rapid descending of the stratification interface, leading to a reduction in the bed expansion, as shown in Fig. 17d and Fig. 19d. The separation remains visible and sits at $Y = 1.10D$ after 360 s. Meanwhile, more bubbles of larger size emerge from the interface and create a vigorous bubbling flow in the dilute region, even though the depth is much shorter than the ones created under smaller amplitudes. Besides, the increasing of amplitude also promotes the packing of solids in the bottom bed, forming a more densely packed stagnant region, as shown in Fig. 18 with a ε of 0.20. The results demonstrate that vibration of a large amplitude enhances both nucleation of bubbles and also the overall packing of solids in the bed. The comparisons above of the beds at increasing Γ demonstrate that Γ alone is not sufficient to govern the hydrodynamics induced in vibro-fluidized beds. Increasing either amplitude or frequency separately leads to increased vibration strength, but results in dramatically different flow patterns and effects on bed hydrodynamics.

In addition, bubble size increases with increasing amplitude, when keeping the vibration unchanged at $f = 10$ Hz. Fig. 20 and Table 3 demonstrate that the tiny bubbles still dominate, yet the amount of larger bubble increases with increasing amplitude from 0.5 mm to 2.0 mm. At $A = 0.5$ mm, the vibration is insufficient to develop any dilute region. As a result, bubbles only form locally in a smaller size, and rise within the gas channels. As the amplitude is increased, channels collapse, and the dilute region develops. Bubbles appear under this vibration, and effectively activate the upper bed. In particular, the overall dilute region created at $A = 1.5$ mm is much larger than that at $A = 1.0$ mm. At a higher amplitude $A = 2.0$ mm, the dilute bed contracts, it yet yields frequently bubbles of larger size.

Consequently, the maximum bed expansion appears at $A = 1.5$ mm, while a similar bed height is attained at $A = 0.5$ mm and $A = 2.0$ mm. Large vibration amplitudes decrease the overall bed expansion, and compact the stagnant region, despite the enhanced bubbling in the dilute region. However, a too-low amplitude hardly breaks up the channels, and the fluidization is not properly assisted.

It becomes clear that, subject to sufficiently powerful vertical vibrations, smooth bubbling fluidization of cohesive powder is attainable. For the micron-silica used here, our recent work [54] has demonstrated that vibration promotes fluidization via activating powders, destabilizing internal structures, and collapsing existing channels, rather than effectively breaking up agglomerates. Simultaneously, vibration also facilitates powder stratification as well as packing. Without supplying any gas, 10 min of vibration at $f = 30$ Hz and $A = 1$ mm condenses the powder bed from loose packing towards a close packing state, resulting in a solid phase that is 5 % denser, similar to the tapping effect observed in a dense granular system [55]. The bottom bed, where the powder experiences the most powerful impact due to collisions with the distributor plate, develops a densely packed solid structure over time, which is robust to the vibration. Under the tested vibration conditions, the powder within the stagnant region remains de-fluidized and immobile, constituting 20 % of the initial packing. Nevertheless, once the fluidization is triggered, vibration also leads to stratification of particles, with the development of an interface between the dilute and dense region, and propagates downwards from the top bed gradually. The only portion of powder fluidized properly is located within the dilute region, which corresponds to 40 % of the powder. Varying vibration settings shows different levels of mitigating the propagation, but not preventing the stratification from occurring. Therefore, processes of long-term fluidization still show similar challenges of sustaining the dilute region. Furthermore, since the vibration propagates via dissipative collisions between particles, its strength decays throughout the bed depth. These witnessed flow patterns indicate the necessity of implementing other assistance approaches in combination with mechanical vibration, such as gas pulsation, jet, or stirring, in order to activate powders in the stagnant and dense regions.

4. Conclusion

Fluidization of cohesive micron-silica powders is observed to be highly dependent on the intensity of external assistance, which is the vertical vibration in this study. Due to the cohesive nature and bed dimension, multiple curved, slender cracks tend to originate from the distributor plate, and then merge into several large gas channels, known as rat holes. The assistance of mechanical vibration significantly enhances interphase contact and destabilizes persistent gas channels, transforming channeling behavior towards bubbling fluidization comparable to the behavior of fluidized Geldart A powders.

However, it should be noted that the induced fluidization is significantly inhomogeneous. The experiments show that vibro-fluidized beds are characterized by three different dynamic flow regions, that are a stagnant region of immobile particles, a dense region of local gas channeling, and a dilute region of vigorous gas bubbling. It becomes clear that common measurements, such as bed expansion and pressure drop, should be interpreted with extra care, as they tend to overestimate the improvement induced.

Increasing vibration frequency yields a more positive impact on fluidization than that of increasing vibration amplitude. A higher frequency (30 Hz in this study) favors fluidization by creating rapid rising bubbles and a significantly dilated dilute region of powders, while a too-large amplitude (2.0 mm in this study) contracts the top bed, eventually leading to a reduced depth of the dilute region. Generally, increasing the magnitude of assistance compacts the solids, and creates a denser stagnant region in proximity to the distributor plate. Therefore, in the long term, the system still degrades into a state of partial fluidization under vibration. Consequently, increasing either amplitude or frequency solely strengthens the vibration, but exhibits different impacts on the flow patterns. This finding suggests that using only vibration strength Γ is very limited when investigating the vibro-fluidization of cohesive powders.

Nevertheless, more powerful vibration is required in systems of larger dimensions, as the strength decays via dissipative collisions among powder vertically throughout the bed. It is yet mechanically challenging to scale up vibration assistance. Therefore, other assistance approaches with the particular target to activate the powder in the bottom regions is preferable to couple with mechanical vibration to impose a more comprehensive influence on the gas channel and solid packing, in order to ensure a stable and effective assistance.

Declaration of Competing Interest

The authors declare that they have no known competing financial interests or personal relationships that could have appeared to influence the work reported in this paper.

Data availability

Data will be made available on request.

Acknowledgements

The research leading to these results has received funding from BASF SE and the Dutch Research Council (NWO) (ENPPS.LIFT.019.027).

Appendix A. Supplementary data

Supplementary data to this article can be found online at https://doi.org/10.1016/j.cej.2023.143936.

References

[1] J.R. van Ommen, J.M. Valverde, R. Pfeffer, Fluidization of nanopowders: a review, J. Nanopart. Res. 14 (3) (2012) 737, https://doi.org/10.1007/s11051-012-0737-4.

[2] F. Raganati, R. Chirone, P. Ammendola, Gas-solid fluidization of cohesive powders, Chem. Eng. Res. Des. 133 (2018) 347–387, https://doi.org/10.1016/j.cherd.2018.03.034.

[3] Z. Zhao, D. Liu, J. Ma, X. Chen, Fluidization of nanoparticle agglomerates assisted by combining vibration and stirring methods, Chem. Eng. J. 388 (2020), 124213, https://doi.org/10.1016/j.cej.2020.124213.

[4] R. Kamphorst, K. Wu, S. Salameh, G.M.H. Meesters, J.R. van Ommen, On the fluidization of cohesive powders: Differences and similarities between micro- and nano-sized particle gas–solid fluidization, Can. J. Chem. Eng. 101 (1) (2023) 227–243, https://doi.org/10.1002/cjce.24615.

[5] J.R. van Ommen, J. Nijenhuis, M.-O. Coppens, Reshaping the structure of fluidized beds, Chem. Eng. Prog. (2009) 49–57.

[6] V. Francía, K. Wu, M.-O. Coppens, Dynamically structured fluidization: oscillating the gas flow and other opportunities to intensify gas-solid fluidized bed operation, Chem. Eng. Process. - Process Intesif. 159 (2021), 108143, https://doi.org/10.1016/j.cep.2020.108143.

[7] M.A.A. Cruz, M.L. Passos, W.R. Ferreira, Final drying of whole milk powder in vibrated-fluidized beds, Drying Technol. 23 (9–11) (2005) 2021–2037, https://doi.org/10.1080/07373930500210473.

[8] H. Khosravi Bizhaem, H. Basirat Tabrizi, Experimental study on hydrodynamic characteristics of gas-solid pulsed fluidized bed, Powder Technol. 237 (2013) 14–23, https://doi.org/10.1016/j.powtec.2013.01.001.

[9] A. Kariman, V. Rao, M. Farjpourlar, Fluidization characteristics of nano particles with the assist of stirrer, IOSR J. Appl. Phys. 5 (2013) 24–27.

[10] R. Hong, J. Ding, H. Li, Fluidization of fine powders in fluidized beds with an upward or a downward air jet, Particuology 3 (3) (2005) 181–186, https://doi.org/10.1016/S1672-2515(07)60083-9.

[11] J.R. van Ommen, D.M. King, A. Weimer, R. Pfeffer, B. van Wachem, S. Johnson, N. Looije, Experiments and modelling of micro-jet assisted fluidization of nanopowder, in: P. E. T. Knowlton (Ed.), 10th international conference on circulating fluidized beds and fluidization technology (CFB-10), ECI Symposium Series, 2013. URL https://dc.engconfintl.org/cfb10/43.

[12] J.A. Quevedo, A. Omosebi, R. Pfeffer, Fluidization enhancement of agglomerates of metal oxide nanopowders by microjets, AIChE J 56 (6) (2010) 1456–1468, https://doi.org/10.1002/aic.12075.

[13] S. Alavi, B. Caussat, Experimental study on fluidization of micronic powders, Powder Technol. 157 (1) (2005) 114–120, https://doi.org/10.1016/j.powtec.2005.05.017.

[14] Y. Zhou, J. Zhu, Group C+ particles: enhanced flow and fluidization of fine powders with nano-modulation, Chem. Eng. Sci. 207 (2019) 653–662, https://doi.org/10.1016/j.ces.2019.06.056.

[15] S.-W. Yin, L. Wang, C.-P. Liu, Study on agglomerate breaking and feeding of superfine particles in fluidized bed, Chin. J. Process Eng. 8 (2) (2008) 230.

[16] J.M. Valverde, A. Castellanos, M.A.S. Quintanilla, Effect of vibration on the stability of a gas-fluidized bed of fine powder, Phys. Rev. E 64 (2001), 021302, https://doi.org/10.1103/PhysRevE.64.021302.

[17] T. Zhou, H. Ogura, M. Yamamura, H. Kage, Bubble motion pattern and rise velocity in two-dimensional horizontal and vertical vibro-fluidized beds, Can. J. Chem. Eng. 82 (2) (2004) 236–242, https://doi.org/10.1002/cjce.5450820204.

[18] E. Marco, A. Santos, M. Menéndez, J. Santamaría, Fluidization of agglomerating particles: influence of the gas temperature and composition on the fluidization of a Li/Mgo catalyst, Powder Technol. 92 (1) (1997) 47–52, https://doi.org/10.1016/S0032-5910(97)03215-4.

[19] D. Barletta, M. Poletto, Aggregation phenomena in fluidization of cohesive powders assisted by mechanical vibrations, Powder Technol. 225 (2012) 93–100, https://doi.org/10.1016/j.powtec.2012.03.038.

[20] T. Zhou, H. Kage, H. Li, Bubble characteristics in a two-dimensional vertically vibro-fluidized bed, Particuol. 3 (4) (2005) 224–228, https://doi.org/10.1016/S1672-2515(07)60191-2.

[21] C. Xu, J. Zhu, Parametric study of fine particle fluidization under mechanical vibration, Powder Technol. 161 (2) (2006) 135–144, https://doi.org/10.1016/j.powtec.2005.10.002.

[22] Z. Wang, M. Kwauk, H. Li, Fluidization of fine particles, Chem. Eng. Sci. 53 (3) (1998) 377–395, https://doi.org/10.1016/S0009-2509(97) 00280-7.

[23] M.A.S. Quintanilla, J.M. Valverde, A. Castellanos, D. Lepek, R. Pfeffer, R.N. Dave, Nanofluidization as affected by vibration and electrostatic fields, Chem. Eng. Sci. 63 (22) (2008) 5559–5569, https://doi.org/10.1016/j.ces.2008.08.012.

[24] C.H. Nam, R. Pfeffer, R.N. Dave, S. Sundaresan, Aerated vibrofluidization of silica nanoparticles, AIChE J 50 (8) (2004) 1776–1785, https://doi.org/10.1002/aic.10237.

[25] S.E. Lehmann, E.U. Hartge, A. Jongsma, I.M. deLeeuw, F. Innings, S. Heinrich, Fluidization characteristics of cohesive powders in vibrated fluidized bed drying at low vibration frequencies, Powder Technol. 357 (2019) 54–63, https://doi.org/10.1016/j.powtec.2019.08.105.

[26] S.E. Lehmann, T. Oesau, A. Jongsma, F. Innings, S. Heinrich, Material specific drying kinetics in fluidized bed drying under mechanical vibration using the reaction engineering approach, Adv. Powder Technol. 31 (12) (2020) 4699–4713, https://doi.org/10.1016/j.apt.2020.11.006.

[27] J. Hartig, A. Shetty, D.R. Conklin, A.W. Weimer, Aeration and cohesive effects on flowability in a vibrating powder conveyor, Powder Technol. 408 (2022), 117724, https://doi.org/10.1016/j.powtec.2022.117724.

[28] E.K. Levy, B. Celeste, Combined effects of mechanical and acoustic vibrations on fluidization of cohesive powders, Powder Technol. 163 (1) (2006) 41–50, https://doi.org/10.1016/j.powtec.2006.01.004.

[29] S. Kaliyaperumal, S. Barghi, L. Briens, S. Rohani, J. Zhu, Fluidization of nano and sub-micron powders using mechanical vibration, Particuology 9 (3) (2011) 279–287, https://doi.org/10.1016/j.partic.2011.03.003.

[30] W. Zhang, A review of techniques for the process intensification of fluidized bed reactors, Chin. J. Chem. Eng. 17 (4) (2009) 688–702, https://doi.org/10.1016/S1004-9541(08)60264-5.

[31] Y. Makkawi, P. Wright, Fluidization regimes in a conventional fluidized bed characterized by means of electrical capacitance tomography, Chem. Eng. Sci. 57 (13) (2002) 2411–2437, https://doi.org/10.1016/S0009-2509(02)00138-0.

[32] T.C. Chandrasekera, A. Wang, D.J. Holland, Q. Marashdeh, M. Pore, F. Wang, A. J. Sederman, L.S. Fan, L.F. Gladden, J.S. Dennis, A comparison of magnetic resonance imaging and electrical capacitance tomography: an air jet through a bed of particles, Powder Technol. 227 (2012) 86–95, https://doi.org/10.1016/j.powtec.2012.03.005.

[33] C.M. Boyce, N.P. Rice, A. Ozel, J.F. Davidson, A.J. Sederman, L.F. Gladden, S. Sundaresan, J.S. Dennis, D.J. Holland, Magnetic resonance characterization of coupled gas and particle dynamics in a bubbling fluidized bed, Phys. Rev. Fluids 1 (7) (2016), 074201, https://doi.org/10.1103/PhysRevFluids.1.074201.

[34] A. Penn, C.M. Boyce, N. Conzelmann, G. Bezinge, K.P. Pruessmann, C.R. Müller, Real-time magnetic resonance imaging of fluidized beds with internals, Chem. Eng. Sci. 198 (2019) 117–123, https://doi.org/10.1016/j.ces.2018.12.041.

[35] R.F. Mudde, Time-resolved x-ray tomography of a fluidized bed, Powder Technol. 199 (1) (2010) 55–59, https://doi.org/10.1016/j.powtec.2009.04.021.

[36] J. R. van Ommen, R. F. Mudde, International Journal of Chemical Reactor Engineering 6 (1). doi:10.2202/1542-6580.1796.

[37] I. Mema, E.C. Wagner, J.R. van Ommen, J.T. Padding, Fluidization of spherical versus elongated particles - experimental investigation using X-ray tomography, Chem. Eng. J. 397 (2020), 125203, https://doi.org/10.1016/j.cej.2020.125203.

[38] S. Maurer, E.C. Wagner, J.R. van Ommen, T.J. Schildhauer, S.L. Teske, S.M. A. Biollaz, A. Wokaun, R.F. Mudde, Influence of vertical internals on a bubbling fluidized bed characterized by X-ray tomography, Int. J. Multiph. Flow 75 (2015) 237–249, https://doi.org/10.1016/j.ijmultiphaseflow.2015.06.001.

[39] A. Helmi, E.C. Wagner, F. Gallucci, M. van Sint Annaland, J.R. van Ommen, R. F. Mudde, On the hydrodynamics of membrane assisted fluidized bed reactors using X-ray analysis, Chem. Eng. Process. 122 (2017) 508–522, https://doi.org/10.1016/j.cep.2017.05.006.

[40] J. Ma, J.R. van Ommen, D. Liu, R.F. Mudde, X. Chen, E.C. Wagner, C. Liang, Fluidization dynamics of cohesive Geldart B particles. part I: X-ray tomography analysis, Chem. Eng. J. 359 (2019) 1024–1034, https://doi.org/10.1016/j.cej.2018.11.082.

[41] J. Gómez-Herńandez, S. Sánchez-Delgado, E. Wagner, R.F. Mudde, J.R. van Ommen, Characterization of TiO_2 nanoparticles fluidization using X-ray imaging and pressure signals, Powder Technol. 316 (2017) 446–454, fluidization for Emerging Green Technologies. doi:10.1016/ j.powtec.2016.11.068.

[42] D. Macrì, S. Sutcliffe, P. Lettieri, Fluidized bed sintering in TiO_2 and coke systems, Chem. Eng. J. 381 (2020), 122711, https://doi.org/10.1016/j.cej.2019.122711.

[43] S. Iannello, P.U. Foscolo, M. Materazzi, Investigation of single particle devolatilization in fluidized bed reactors by X-ray imaging techniques, Chem. Eng. J. 431 (2022), 133807, https://doi.org/10.1016/j.cej. 2021.133807.

[44] J. Saayman, W. Nicol, J.R. van Ommen, R.F. Mudde, Fast x-ray tomography for the quantification of the bubbling-, turbulent- and fast fluidization-flow regimes and void structures, Chem. Eng. J. 234 (2013) 437–447, https://doi.org/10.1016/j.cej.2013.09.008.

[45] D. Gidaspow, R. Bezburuah, J. Ding, Hydrodynamics of circulating fluidized beds: Kinetic theory approach, in: Proc. of 7th Eng. Found. Conf. on Fluidization, 1991, pp. 75–82.URL https://www.osti.gov/biblio/5896246.

[46] H.M. Beakawi Al-Hashemi, O.S. Baghabra Al-Amoudi, A review on the angle of repose of granular materials, Powder Technol. 330 (2018) 397–417, https://doi.org/10.1016/j.powtec.2018.02.003.

[47] J.R. van Ommen, S. Sasic, J. van der Schaaf, S. Gheorghiu, F. Johnsson, M.-O. Coppens, Time-series analysis of pressure fluctuations in gassolid fluidized beds - A review, Int. J. Multiph. Flow 37 (5) (2011) 403–428, https://doi.org/10.1016/j.ijmultiphaseflow.2010.12.007.

[48] K. Wu, F. Galli, J. de Tommaso, G.S. Patience, J.R. van Ommen, Experimental methods in chemical engineering: pressure, Can. J. Chem. Eng. 101 (1) (2023) 41–58, https://doi.org/10.1002/cjce.24533.

[49] A.P. Baskakov, V.G. Tuponogov, N.F. Filippovsky, A study of pressure fluctuations in a bubbling fluidized bed, Powder Technol. 45 (2) (1986) 113–117, https://doi.org/10.1016/0032-5910(66)80003-7.

[50] F. Melo, P. Umbanhowar, H.L. Swinney, Transition to parametric wave patterns in a vertically oscillated granular layer, Phys. Rev. Lett. 72 (1994) 172–175, https://doi.org/10.1103/PhysRevLett.72.172.

[51] D. Bradley, G. Roth, Adaptive thresholding using the integral image, J. Graphics Tools 12 (2) (2007) 13–21, https://doi.org/10.1080/2151237X. 2007.10129236.

[52] Y. Mawatari, Y. Tatemoto, K. Noda, Prediction of minimum fluidization velocity for vibrated fluidized bed, Powder Technol. 131 (1) (2003) 66–70, https://doi.org/10.1016/S0032-5910(02)00323-6.
[53] C. Ma, H. Xu, W. Zhong, W. Wang, H. Zhang, Experimental study on fluidization characteristics of vinegar residue in a vibrated fluidized bed, Adv. Powder Technol. 33 (8) (2022), 103698, https://doi.org/10.1016/j. apt.2022.103698.
[54] R. Kamphorst, P.C. van der Sande, K. Wu, E.C. Wagner, M. David, G.M.H. Meester, J.R. van Ommen, The mechanism behind vibration assisted fluidization of cohesive micro-silica, Kona Powder Part. J. (2023), https://doi.org/10.14356/kona.2024007. In press.
[55] C. Josserand, A.V. Tkachenko, D.M. Mueth, H.M. Jaeger, Memory effects in granular materials, Phys. Rev. Lett. 85 (2000) 3632–3635, https://doi.org/10.1103/PhysRevLett.85.3632.